A microstructure-based parameterization of the effective, anisotropic elasticity tensor of snow, firn, and bubbly ice

Kavitha Sundu[1], Johannes Freitag[2], Kévin Fourteau[1,3], and Henning Löwe[1]

[1]WSL Institute for Snow and Avalanche Research SLF, Davos, Switzerland
[2]Alfred-Wegener-Institut, Helmholtz-Zentrum für Polar- und Meeresforschung, Bremerhaven, Germany
[3]Univ. Grenoble Alpes, CNRS, IRD, Grenoble INP, IGE, 38000 Grenoble, France

Correspondence: H. Löwe (loewe@slf.ch)

Abstract. Quantifying the link between microstructure and effective elastic properties of snow, firn, and bubbly ice is essential for many applications in cryospheric sciences. The microstructure of snow and ice can be characterized by different types of fabrics (crystallographic, geometrical), which gives rise to macroscopically anisotropic elastic behavior. While the impact of the crystallographic fabric has been extensively studied in deep firn, the present work investigates the influence of the geometrical fabric over the entire range of possible volume fractions. To this end, we have computed the effective elasticity tensor of snow, firn, and ice by finite element simulations based on 391 X-ray tomography images comprising samples from the laboratory, Alps, Greenland, and Antarctica. We employed a variant of the Eshelby tensor that has been previously utilized for the parametrization of thermal and dielectric properties of snow and utilized Hashin-Shtrikman bounds to capture the nonlinear interplay between density and geometrical anisotropy. From that we derive a closed-form parametrization for all components of the (transverse isotropic) elasticity tensor for all volume fractions using 2 fit parameters per tensor component. Finally, we used the Thomsen parameter to compare the geometrical anisotropy to the maximal theoretical crystallographic anisotropy in bubbly ice. While the geometrical anisotropy is clearly dominating up to ice volume fractions of $\phi \approx 0.7$, a thorough understanding of elasticity in bubbly ice may require a coupled elastic theory that includes geometrical *and* crystallographic anisotropy.

Copyright statement. TEXT

1 Introduction

The elastic modulus can be used to represent the mechanical property of snow, firn or ice and the knowledge of the effective elasticity tensor plays a crucial role in a variety of applications throughout the field of cryospheric sciences. Examples comprise micromechanical modeling of snow compaction (Wautier et al., 2016), fracture propagation in weak layers for slab avalanche release (Gaume et al., 2013; Bobillier et al., 2020), or the interpretation of near-surface (Chaput et al., 2022) or deep firn (Diez and Eisen, 2015; Diez et al., 2015; Schlegel et al., 2019) seismic signatures through the link between wave velocities and elastic moduli.

The work of Schlegel et al. (2019) emphasized the role of elastic anisotropy. Specifically, the retrieval of elasticity profiles of snow, firn, and ice through seismic waves usually relies on the assumption of isotropy which constitutes an uncertainty in the inversion method. Snow and firn are however known to be anisotropic due to both the ice matrix geometry (e.g., Löwe et al., 2013; Calonne et al., 2015; Leinss et al., 2016; Moser et al., 2020; Montagnat et al., 2020), and the crystallographic orientations of the ice crystals (e.g., Diez et al., 2015; Petrenko and Whitworth, 1999b). The geometrical anisotropy arises from the geometrical orientation of the structure that constitutes the ice matrix in snow (for instance if it is predominantly orientated towards the vertical direction), while the crystallographic anisotropy is an inherent characteristic of the ice crystals themselves. While the geometrical fabric in firn is strong (leading to a strong geometrical elastic anisotropy) near the surface due to temperature gradient metamorphism (Montagnat et al., 2020) and decays with depth (Fujita et al., 2014), the crystallographic fabric is weak near the surface (thus yielding a weak crystallographic elastic anisotropy) but increases with depth under densification and flow (e.g., Montagnat et al., 2014; Saruya et al., 2022). Recent work by Hellmann et al. (2021) on measuring wave propagation in glacier ice suggests that even at low porosity ($< 1\%$), the effective elastic (crystallographic) anisotropy of polycrystalline ice is influenced by the geometrical effects of the porosity.

The estimation of the geometrical anisotropy usually relies on advanced microstructural characterization, such as the estimation correlation lengths (Krol and Loewe, 2016). Despite its complexity, this microstructural characterization of snow, firn and ice has become a standard worldwide in the last decade thanks to the development of micro-computed tomography (μCT) in the US (Baker, 2019), Japan (Ishimoto et al., 2018), India (Srivastava et al., 2016), Norway (Salomon et al., 2022), Germany (Freitag et al., 2004), France (Wautier et al., 2015) and Switzerland (Köchle and Schneebeli, 2014). The increasing role played by the microstructural characterization of snow and firn, fostered by μCT, led to the development of alternative retrieval methods, such as the characterization of anisotropy from radar (Leinss et al., 2016).

For snow, the impact of the geometrical anisotropy has been studied (Srivastava et al., 2016) only in a limited range of porosities. Thus, a parameterization of the elastic modulus, based on density and geometrical anisotropy for the entire possible range of porosities would constitute a first step towards understanding this concurrent anisotropy problem. This could have immediate applications, e.g., for retrieving sub-surface density and anisotropy through seismics using advanced inversion methods (Wu et al., 2022). Leinss et al. (2016) show that an electromagnetic inversion model could be exploited to retrieve the geometrical anisotropy of snow, and this despite a sub-dominant impact of the geometrical anisotropy on the effective permittivity tensor. A better understanding of the link between geometrical and elastic anisotropy would thus enable the use of a similar technique to retrieve the geometrical anisotropy of snow from seismic surveys.

The effective elasticity tensor of snow, firn, or ice can be directly obtained through numerical homogenization on micro-tomography images. Using Finite-Element (FE) methods via volume averaging, a solution for static linear elasticity yields the material effective elastic properties. Here, it is commonly assumed that the ice matrix is isotropic, polycrystalline ice with known bulk and shear modulus (see Garboczi, 1998; Köchle and Schneebeli, 2014; Wautier et al., 2015). It has been recently confirmed that the effective elastic properties obtained by microstructure based FE agree well with acoustic measurements (Gerling et al., 2017). Though straightforward, the microstructure-based FE approach is computationally expensive and requires the microstructure to be known. Therefore, accurate parametrizations are still highly desirable and presently no

parametrization of the effective elastic modulus exist that can be consistently applied without making a restriction to a limited range of volume fractions.

As an alternative to numerical simulations, it is often helpful to consider effective medium theories and rigorous approximations. Rigorous bounds such as Hashin-Shtrikman (HS) bounds (Hashin and Shtrikman, 1962) can be used to approximate the elastic properties of porous materials (Torquato, 1991). Although bounds are widely known to be inaccurate predictors of the elastic properties in absolute value (Roberts and Garboczi, 2002), the HS bounds incorporate the non-linear interplay between structural anisotropy via the Eshelby tensor and density (Torquato, 2002b) and they have the correct limiting behavior for small and large volume fractions. These properties can be systematically exploited for constructing more sophisticated parametrizations.

The present work aims to derive a parameterization of the effective elasticity tensor of snow, firn, and bubbly ice based on volume fraction and structural anisotropy and that can be consistently applied to the entire range of volume fractions. We achieve this by taking the anisotropic HS bounds (without free parameter) as the functional starting point and by using an empirical transformation (containing two fit parameters per tensor component). The proposed fitting function matches observed characteristic features, namely the power-law increase of the moduli for high porosities (for snow) and the asymptotic behavior of dilute sphere dispersions (for bubbly ice) in the limit of low porosities.

The paper is organized as follows. Section 2 gives the background on the elasticity theory, examines the limitation of existing parameterizations, and motivates the methodological idea that underlies the proposed parameterization for the elasticity tensor. Section 3 presents an overview of the 391 tomography samples that were used, and the methods that are employed to calculate correlation functions, fabric tensors, FE simulations, and fitting procedures for estimating the free parameters in the elasticity formulas. In Sect. 4 we show performance of new parameterization, by comparing it with previous work in which these parameters are not captured. Finally, we discuss in Sect. 5 the expected interplay between crystallographic and geometrical anisotropy for the elastic modulus for snow, firn, and ice and conclude in Sect. 6.

2   Theoretical background

2.1   The effective elasticity tensor

Snow is a heterogeneous and porous material with an ice volume fraction ϕ (defined as the ratio between the volume occupied by the ice phase over that of the sample), whose effective, macroscopic properties can be computed by volume averaging over a sufficiently large volume, known as representative volume element (RVE) (see Hill, 1963; Hashin, 1963; Nemat-Nasser and Hori, 1995; Torquato, 1997; Willis, 1981). The effective (fourth order) elasticity tensor C of a statistically homogenous two-phase composite material is defined by Hooke's law, using Hill's lemma, of elasticity as

$$\langle \boldsymbol{\sigma} \rangle = \boldsymbol{C} : \langle \boldsymbol{\varepsilon} \rangle, \tag{1}$$

that relates the volume averaged second-order stress $\langle \boldsymbol{\sigma} \rangle$ and strain tensors $\langle \boldsymbol{\varepsilon} \rangle$, given in Voigt notation as $[\sigma_{11}, \sigma_{22}, \sigma_{33}, \sigma_{13}, \sigma_{23}, \sigma_{12}]^T$ and $[\varepsilon_{11}, \varepsilon_{22}, \varepsilon_{33}, 0.5\varepsilon_{13}, 0.5\varepsilon_{23}, 0.5\varepsilon_{12}]^T$, respectively. Angular brackets denote volume averaging over a statistically homo-

geneous region of interest and makes the connection between the volume averaged strain energy of a heterogeneous material at the microscopic scale and that of a macroscopically heterogeneous material under uniform strain. The operator : denotes double contraction (Torquato, 1997). We consider snow to be a transversely isotropic (TI) material, where the axis of transverse symmetry is chosen as the vertical z- axis perpendicular to the horizontal isotropic xy- plane. The elasticity tensor of a TI material can be described by 5 independent moduli. Using Voigt notation, it can be written (Torquato, 2002a) as a symmetric 6×6 matrix as

$$
\boldsymbol{C} = \begin{bmatrix} C_{11} & C_{12} & C_{13} & 0 & 0 & 0 \\ C_{12} & C_{11} & C_{13} & 0 & 0 & 0 \\ C_{13} & C_{13} & C_{33} & 0 & 0 & 0 \\ 0 & 0 & 0 & C_{44} & 0 & 0 \\ 0 & 0 & 0 & 0 & C_{44} & 0 \\ 0 & 0 & 0 & 0 & 0 & \frac{1}{2}(C_{11} - C_{12}) \end{bmatrix}. \tag{2}
$$

For an isotropic material the number of independent entries reduces to two, e.g., the shear modulus $G = C_{44}$ and the P-wave modulus C_{33}. Wherever necessary, the common relations are employed (Torquato, 2002a) to connect to alternative formulations in terms of Young's modulus E, bulk modulus K, shear modulus G and Poisson's ratio ν (see Appendix A).

To quantify the deviation from elastic isotropy, it is common to use the so called Thomsen parameter ϵ, which is a dimensionless quantity defined as (see Thomsen, 1986)

$$
\epsilon = \frac{C_{11} - C_{33}}{2C_{33}}. \tag{3}
$$

For an isotropic material, the Thomsen parameter ϵ is zero. Throughout this work, we consider the elastic properties of snow/firn at a given instant in time, where the microstructure gives pointwise information about the position of ice and air. We do not consider any underlying time-dependent process that would result in the evolution of the microstructure (such as metamorphism).

2.2 Isotropic parametrizations based on ice volume fraction

2.2.1 Snow: Power law models

For applications, the elastic moduli must be related to accessible parameters of snow. The most common way are empirical parameterizations based on ice volume fraction ϕ, that is equivalent to density. Such density-based parameterizations use a power law (Frolov and Fedyukin, 1998; Sigrist, 2006; Gerling et al., 2017) or exponential relationships (Köchle and Schneebeli, 2014; Scapozza, 2004) to comply with the observed drastic increase of elasticity of snow with increasing density. The different density based parametrizations for low density snow have been compared in many publications (e.g., Köchle and Schneebeli, 2014). For the purpose of the present paper we choose one example, namely the power-law parameterization from Gerling et al. (2017) as it was derived from microstructure based FE simulations (as in this study) and experiments. We write the

parametrization in the form

$$C_{ij}^{\mathrm{G}}(\phi) = a_{ij}\phi^{b_{ij}},\tag{4}$$

where C_{ij}^{G} are the components of the elasticity tensor, a_{ij} and b_{ij} are the empirical parameters. They need to be estimated by fitting experimental data and FE simulations, employing Eq. 4 in an optimization procedure (Gerling et al., 2017). In Gerling et al. (2017) only the C_{33} component was computed through optimization procedure with FE simulations and led to $a_{33} = 6 \cdot 10^{-10}$ and $b_{33} = 4.6$ for snow with volume fractions in the range $0.1 < \phi < 0.4$.

2.2.2 Firn: Kohnen parametrization

A conceptually similar parametrization, however valid for an entirely different range of ice volume fractions, can be inferred from the parametrization of acoustic wave velocities in firn. Kohnen (1972) has derived an empirical relationship between the S and P wave velocities in (isotropic) firn and the density. By relating wave velocities to the respective elastic moduli via density, the Kohnen relations can be cast into an ice volume fraction based parametrization for the S and P wave modulus (C_{33} and C_{44} components of the elastic modulus) which are valid in low porosity firn. Based on the original work, we rewrite the Kohnen empirical formula in the form

$$C_{ij}^{\mathrm{KOH}}(\phi) = \rho\left[v_{ij}^{\mathrm{ice}} - \alpha_{ij}\left(\frac{1}{\phi}-1\right)^{1/\beta_{ij}}\right]^2,\tag{5}$$

with the empirical parameters proposed by Kohnen (1972): $\alpha_{33} = 2250\,\mathrm{m\,s^{-1}}$, $\beta_{33} = 1.22$, $\alpha_{44} = 950\,\mathrm{m\,s^{-1}}$, and $\beta_{44} = 1.17$, and the P-wave and S-wave velocities in ice $v_{33}^{\mathrm{ice}} = 3900$ and $v_{44}^{\mathrm{ice}} = 2100$ given in units $\mathrm{m\,s^{-1}}$. The P-wave and S-wave velocities are provided by Diez (2013) and applies for ice volume fractions ranging from 0.43 to 0.98. Yet, the Kohnen parameterization is supposed to work best after the firn-ice transition, i.e. for ϕ ranging from 0.88 to 0.98 (Diez, 2013).

2.2.3 Ice: Exact limit for dilute dispersions of spheres

For bubbly ice at very low porosities ($0.9 < \phi < 1$), the air phase can be commonly described as isolated, nearly spherical bubbles (e.g., Fourteau et al., 2019). This limiting case can be addressed analytically by considering a dilute dispersion of spherical cavities with vanishing stiffness ($K^{\mathrm{air}} = G^{\mathrm{air}} = 0$) in ice (Torquato, 1991). In this limit, the effective elastic modulus C^{DDS} can be computed exactly (Torquato, 2002a) and, due to isotropy, determined from the effective bulk modulus K^{DDS} and shear modulus G^{DDS} given by

$$
\begin{aligned}
C_{ij}^{\mathrm{DDS}} &= 3K^{\mathrm{DDS}}(\Lambda_h)_{ij} + 2G^{\mathrm{DDS}}(\Lambda_s)_{ij},\\
K^{\mathrm{DDS}} &= K^{\mathrm{ice}}(1 - \frac{3K^{\mathrm{ice}} + 4G^{\mathrm{ice}}}{4G^{\mathrm{ice}}}(1-\phi)),\\
G^{\mathrm{DDS}} &= G^{\mathrm{ice}}(1 - \frac{G^{\mathrm{ice}} + H^{\mathrm{ice}}}{H^{\mathrm{ice}}}(1-\phi)),
\end{aligned}\tag{6}
$$

where

$$H^{\mathrm{ice}} \equiv G^{\mathrm{ice}}(\frac{3K^{\mathrm{ice}}/2 + 4G^{\mathrm{ice}}/3}{K^{\mathrm{ice}} + 2G^{\mathrm{ice}}}).\tag{7}$$

Here Λ_h and Λ_s are the hydrostatic and shear projection tensors, respectively, defined in (Torquato, 2002a, Eq. 13.96 and Eq. 13.97) and C_{33}^{DDS} component is given by $K^{\mathrm{DDS}} + 4G^{\mathrm{DDS}}/3$.

2.3 Anisotropic parametrizations based on ice volume fraction and geometrical fabric

145   To overcome the restrictive assumption of isotropic parametrizations it is necessary to extend the microstructural description. Cowin (1985) showed that the elasticity tensor of porous materials can be estimated, based on symmetry arguments, from the morphology and the elastic properties of the matrix phase (Moreno et al., 2016). According to Cowin (1985), the elasticity tensor can be determined as a function of Lamé constants of the porous material, λ and μ, volume fraction ϕ and the fabric tensor $\boldsymbol{M}$ which captures the anisotropy of the material (Moreno et al., 2016). For snow, this was utilized by Srivastava et al.

150   (2016) who used the Zysset–Curnier formulation (Zysset and Curnier, 1995) to incorporate the fabric tensor. This led to a (orthotropic elastic) formulation of the elasticity tensor given by

$$
\begin{aligned}
C_{ij}^{\mathrm{ZC}}(\phi, \boldsymbol{M}) = &\sum_{i=1}^{3} (\lambda + 2\mu)\,\phi^k m_i^{2l} (\boldsymbol{M}_i \otimes \boldsymbol{M}_i) \\
&- \sum_{\substack{i,j=1 \\ i \neq j}}^{3} \lambda' \phi^k m_i^l m_j^l (\boldsymbol{M}_i \otimes \boldsymbol{M}_j) \\
&+ \sum_{\substack{i,j=1 \\ i \neq j}}^{3} 2\mu\,\phi^k m_i^l m_j^l (\boldsymbol{M}_i \overline{\otimes} \boldsymbol{M}_j).
\end{aligned}
\tag{8}
$$

Here m_i denotes the i-th eigenvalues of the positive definite fabric-tensor $\boldsymbol{M}$ and $\boldsymbol{M}_i$ is the projector on the corresponding eigenspace. The dependence on the eigenvalues and the ice volume-fraction ϕ are assumed to be of power-law type charac-

155   terized by the empirical exponents k and l, respectively. This power-law form derives from a polynomial expansion of the elasticity tensor expression in terms of the fabric tensor eigenvalues (Zysset, 2003). The definition of double tensorial product $\boldsymbol{A}\overline{\otimes}\boldsymbol{B}$ is given by (Srivastava et al., 2016).

   Srivastava et al. (2016) derived the fit parameters through optimization procedure, employing Eq. (8) and microstructure based FE simulations with snow samples in the range $0.109 < \phi < 0.59$. The parameters obtained by Srivastava et al. (2016)

160   are $\lambda = 5.33, \lambda' = 5.27, \mu = 9.54, k = 4.69,$ and $l = 2.55$.

2.4 Anisotropic Hashin-Shtrikman bounds

An alternative theoretical approach to the geometrically anisotropic elasticity of heterogeneous materials can be realized through bounds (Hashin and Shtrikman, 1962; Torquato, 1991). When using Hashin–Shtrikman (HS) bounds, the effective elastic properties of porous materials can be estimated based on volume fraction and microstructural geometrical anisotropy

165   (incorporated through n-point correlation functions). This results in tighter bounds over Voigt and Reuss bounds, which are just based on the volume fraction of the material. As the air phase of the snow microstructure has zero elasticity, only the upper

bound $[0 \leq \boldsymbol{C} < \boldsymbol{C}^{\mathrm{U}}]$ is meaningful (Roberts and Garboczi, 2002) and it is given by (Torquato, 2002a)

$$\boldsymbol{C}^{\mathrm{U}} = \boldsymbol{C}^{\mathrm{ice}} - (1-\phi)\phi\boldsymbol{C}^{\mathrm{ice}} : \boldsymbol{P}^{\mathrm{ice}} : \boldsymbol{C}^{\mathrm{ice}} : [\boldsymbol{I} + \phi\boldsymbol{P}^{\mathrm{ice}} : -\boldsymbol{C}^{\mathrm{ice}}]^{-1}, \tag{9}$$

where $\boldsymbol{C}^{\mathrm{U}}$ represents Hashin-Shtrikman upper bound on effective elastic modulus $\boldsymbol{C}$, the components of the fourth-order identity tensor $\boldsymbol{I}$ is given as $I_{pqrs} = (\delta_{pr}\delta_{qs} + \delta_{ps}\delta_{qr})/2$, ϕ is the volume fractions of ice. The bound involves the elasticity tensor $\boldsymbol{C}^{\mathrm{ice}}$ of ice as the host material, which needs to be isotropic for the derivation of Eq. (9). Such an assumption is consistent with our focus on the geometrical, rather than crystallographic, anisotropy and the use of an isotropic material in our FE simulations (see Sec. 3). The bound thus involves the bulk modulus K^{ice} and shear modulus G^{ice} of ice. The tensor $\boldsymbol{P}^{\mathrm{ice}}$ is the polarization tensor, which incorporates the structural anisotropy through aspect ratio α of the correlation lengths (Torquato, 1997). The tensor $\boldsymbol{P}^{\mathrm{ice}}$ is related to the Eshelby tensor $\boldsymbol{S}^{\mathrm{ice}}$ (Eshelby and Peierls, 1957) of the matrix phase via the relation

$$\boldsymbol{P}^{\mathrm{ice}} = \boldsymbol{S}^{\mathrm{ice}} : [\boldsymbol{C}^{\mathrm{ice}}]^{-1}. \tag{10}$$

The Eshelby tensor (see Sect. B) in the Hashin-Shtrikman bounds accounts for the anisotropic "shape" of the microstructure through the geometrical anisotropy ratio α and is the equivalent of the fabric tensor $\boldsymbol{M}$ in the anisotropic ZC model (see Eq. (8)). A geometrical anisotropy ratio $\alpha > 1$ corresponds to predominant vertical orientation of ice matrix (prolate inclusions), $\alpha < 1$ corresponds to predominant horizontal orientation of ice matrix (oblate inclusions), and $\alpha = 1$ corresponds to isotropic distribution of ice matrix. Finally, we note that while both the fabric tensor $\boldsymbol{M}$ in the ZC formulation and the Eshelby tensor $\boldsymbol{S}^{\mathrm{ice}}$ in the HS formulation are used to described structural anisotropy, they cannot be used interchangeably, notably as $\boldsymbol{M}$ is second rank tensor whereas $\boldsymbol{S}^{\mathrm{ice}}$ is a fourth rank tensor.

2.5 Requirements for a consistent elasticity tensor parameterization

The parametrizations and model presented above are all designed for a specific range of validity. To demonstrate the requirements for a consistent parametrization valid for snow, firn, and ice we provide an overview of all models presented above evaluated by using their free parameters as originally published. Figure 1 shows the C_{33} component as a function of volume fraction for all models. For the formulations including geometric anisotropy, three different anisotropy ratios ($\alpha = 0.7, 1,$ and 1.6) were evaluated and the corresponding spread in elastic properties is shown as shaded area for these models.

Due to its simple power law dependence on density, the G parametrization (Gerling et al., 2017) exceeds even the modulus of ice (black square for $\phi = 1$). A very similar behavior is found for the isotropic ZC (Srivastava et al., 2016) variant, demonstrating the consistency of G and ZC for low volume fractions but the failure for high volume fraction. In addition, ZC shows an influence of geometrical anisotropy that increases monotonically with ice volume fraction, which is also nonphysical since in the limit of $\phi \to 1$ the elastic anisotropy behavior of the microstructure must tend to an isotropic state. In contrast, the upper bound C_{33}^{U} correctly approaches the ice limiting value of ice (black square) while the influence of geometrical anisotropy tends to zero. In addition, the U formulation agrees also in the vicinity of $\phi = 1$ with the prediction of dilute dispersion of spherical (DDS) cavities. In contrast, the agreement of U and DDS for $\phi > 0.8$ with the isotropic Kohnen formulation demonstrates the validity of this asymptotic behavior for ice, while in turn KOH naturally fails for low volume fractions (snow) lying outside its range of applicability.
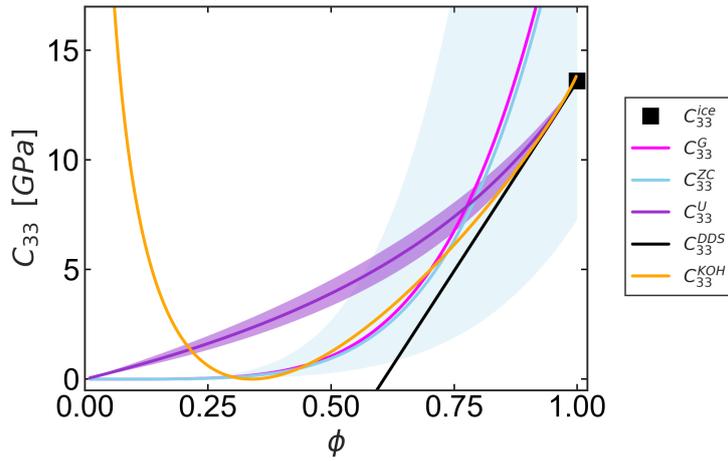
Figure 1. Evolution of the elastic modulus C_{33} as a function of volume fraction ϕ for all discussed models: density based parameterization proposed by Gerling et al. (2017) (C_{33}^G - see Eq. (4); expected range of validity $0.1 < \phi < 0.4$) , band of values predicted by Srivastava et al. (2016) (C_{33}^{ZC} - see Eq. (8); expected range of validity $0.109 < \phi < 0.59$), band of values predicted by the Hashin-Shtrikman upper bound (C_{33}^U - see Eq. (9)), elastic modulus for dilute dispersions (C_{33}^{DDS} - see Eq. (6); valid for high ice volume fractions) and by Kohnen (1972) empirical relationship (C_{33}^{KOH} - see Eq. (5); expected range of validity $0.43 < \phi < 0.98$) are shown as a function of the volume fraction (ϕ) with continuous lines. The black square represents the maximum value of the elastic modulus in C_{33} direction for ice volume fraction $\phi = 1$. The shaded area for the anisotropic models represents the range of values between the two aspect ratios $\alpha = 1.7$ and $\alpha = 0.6$.

2.6 The remedy: Matching asymptotics

The best of all existing models can be combined in a single model by constructing an empirical transition model that i) increases as a power law for low volume fraction ii) includes anisotropy but with vanishing influence when approaching ice iii) approaches the limiting behavior of dilute air bubbles for low porosity. Due to the properties of the HS bounds (correct limiting behavior of the bounds for low and high volume fraction, rational function for intermediate volume fractions) this can be achieved by using a transformation in the following form, in which HS bound C_{ij}^U is normalized by C_{ij}^{ice} as

$$C_{ij}^{PW} = C_{ij}^{ice} f_{ij} \left(\frac{C_{ij}^U}{C_{ij}^{ice}} \right), \tag{11}$$

with an empirical transition function $f_{ij} : [0,1] \to [0,1]$ for each component of the elasticity tensor. Given that the HS bound approaches the dilute dispersion limiting behavior for $x \to 1$ (Hashin and Shtrikman (1962)), the transition functions must obey $f_{ij}(x) \sim x$ for $x \to 1$. Given further, that the modulus increases as a power law for lower volume fractions, the scaling

210   function must behave as $f_{ij}(x) \sim x^{\beta}$ for $x \to 0$. These two asymptotics can be matched in the following empirical form

$$f_{ij}(x) = \frac{x^{\beta}}{\xi(1-x) + x^{\beta-1}} \sim \begin{cases} x^{\beta}/\xi, & \text{for } x \to 0 \\ x, & \text{for } x \to 1, \end{cases} \tag{12}$$

which has the correct asymptotic behavior and contains only 2 free parameters. The first free parameter β ensures that at low volume fraction the modulus increases as a power law of the ice volume fraction. The second free parameter ξ acts, on the one hand, as a modification of the prefactor in the power law and, on the other hand, as the transition scale that controls the

215   crossover to $f(x) \sim x$. Eq. (11) and Eq. (12) together with Eq. (9) constitutes our empirical model that depends on density and anisotropy in a physically consistent way. The corresponding tensor components are henceforth referred to as C_{ij}^{PW} which will be analyzed and parametrized in the following from snow, firn, and ice tomography samples and finite element simulations of the elastic modulus.

3   Material and computational methods

220   ## 3.1   Tomography samples

For the parametrization of snow elastic properties we used 391 microstructure images of snow, firn, and bubbly ice obtained with the help of μCT. Samples are taken from previous work and comprise laboratory, Alpine, Arctic, and Antarctic snow and ice. A brief description is given in Table 1. We considered the full range of porosities ranging from 0.06 - 0.93, and anisotropy ratios α ranging from 0.45-1.87. Note that all samples are cubic, with the same length L in the x, y, and z directions.

Table 1. μCT samples used for the parameterization of the elasticity tensor.

Name (Count)	Description (Location)	ϕ range	α range	Dimension L [mm]	obtained from
TS-TGM2 (45)	Temperature gradient time series (Lab)	0.21 - 0.25	0.76 - 1.18	5.4	
TS-TGM17 (49)	Temperature gradient time series (Lab)	0.30 - 0.32	0.90 - 1.15	7.5	
TS-DH1 (6)	Metamorphism box time series (Lab)	0.175 - 0.31	0.74 - 1.45	10.69	Löwe et al. (2013)
TS-ISO1 (10)	Isothermal time series (Lab)	0.16 - 0.26	0.69 - 1.00	5.11	
TS-ISO5 (10)	Isothermal time series (Lab)	0.16 - 0.24	0.65 - 1.04	5.11	
Alp-DIV (41)	Various Alpine samples (Davos, Switzerland)	0.06 - 0.39	0.56 - 1.67	6.86	
Arc-EGRIP (184)	Snow core (Greenland)	0.24 - 0.66	0.45 - 1.87	10.8	Montagnat et al. (2020)
Ant-B34 (4)	Firn core (Antartica)	0.43 - 0.93	1.07 - 1.11	12.0	Schlegel et al. (2019)
Ant-B54 (32)	Firn core (Antartica)	0.60 - 0.80	1.00 - 1.17	18.0	
Ant-Lock-In (10)	Ice core (Antartica)	0.85 - 0.93	1.05 - 1.12	15.0	Fourteau et al. (2019)

3.2 Correlation functions

We use tomography images of snow to compute the correlation functions of snow microstructures to calculate the anisotropy. As dry snow is a two-phase composite material consisting of air and ice phase, the indicator function $\mathcal{I}(\mathbf{x})$ accounts for the spatial distribution of ice and air and is denoted by

$$\mathcal{I}(\boldsymbol{x}) = \begin{cases} 1 & \text{if } \boldsymbol{x} \in \text{ice} \\ 0 & \text{if } \boldsymbol{x} \in \text{air}. \end{cases} \tag{13}$$

The two-point correlation function $\chi(\boldsymbol{r})$ (Torquato, 2002b) entails information about the phase correlation of the end points of vector $\boldsymbol{r}$ and is defined by

$$\chi(\boldsymbol{r}) = \langle \mathcal{I}(\boldsymbol{x} + \boldsymbol{r})\mathcal{I}(\boldsymbol{x}) \rangle - \phi^2. \tag{14}$$

We assume a statistically homogeneous material, where χ is independent of the reference point $\boldsymbol{x} \in \mathbb{R}^3$. $\chi(\boldsymbol{r})$ is computed from 3D images via Fast Fourier transformation (Krol and Loewe, 2016; Löwe et al., 2013). Correlation lengths ℓ_z, ℓ_x and ℓ_y are obtained by fitting $\chi_q(\boldsymbol{r})$ along the Cartesian coordinate axes $q = x, y$, and z to an exponential function $\chi_q(\boldsymbol{r}) = \chi_{q,0}\exp\left(-r/\ell_q\right)$. From this the geometrical anisotropy parameter is defined by $\alpha = \ell_z/\ell_{xy}$.

3.3 Geometrical fabric tensor

Srivastava et al. (2016) showed that the choice of the fabric tensor $\boldsymbol{M}$ computed either by mean intercept lengths (MIL), star length distributions (SLD), and star volume distribution(SVD) methods did not play a significant role in the computation of the effective elasticity tensor of snow. Therefore, we use the depolarization tensor $\boldsymbol{M}^*$ given by Torquato (2002a), which is based on two-point correlation lengths to estimate the structural anisotropy of the microstructure. Using $\boldsymbol{M}^*$ allows us to connect to previous work (Löwe et al., 2013; Montagnat et al., 2020; Calonne et al., 2015; Leinss et al., 2016) where this orientation tensor was employed to determine the anisotropic effective thermal conductivity and permittivity of snow. Analogous to MIL, $\boldsymbol{M}^*$ is the symmetric depolarization tensor of a 3-dimensional ellipsoid with the eigenvalues in principle axes frame given by elliptical integrals, and its trace is unity (Torquato, 2002a). In the case of transverse isotropy around the z-axis, the depolarization tensor computed from two-point correlation function $\chi(\boldsymbol{r})$ reduces to

$$\boldsymbol{M}^* = \begin{bmatrix} Q(\alpha) & 0 & 0 \\ 0 & Q(\alpha) & 0 \\ 0 & 0 & 1 - 2Q(\alpha) \end{bmatrix}. \tag{15}$$

The definition of the function $Q(\alpha)$ in terms of anisotropy ratio α is given in Sect. C.

3.4 FE simulations

Finite Elements Method (FEM) simulations were performed using the code from Garboczi (1998) on all the CT images to determine the elasticity tensor of the snow microstructure by employing periodic boundary conditions. For these simulations, we assumed elastically isotropic ice with a shear modulus $G^{\text{ice}} = 3.52\,\text{GPa}$ and bulk modulus $K^{\text{ice}} = 8.9\,\text{GPa}$, corresponding to a temperature of $-16°\text{C}$ (Petrenko and Whitworth, 1999b). We performed FE simulations for five load states derived from Cartesian basis vectors in the six-dimensional deformation space. The deformation ε of the five load states are taken from the set $\{\varepsilon_0 e_{11}\,;\,\varepsilon_0 e_{22}\,;\,\varepsilon_0 e_{33}\,;\,\varepsilon_0(e_{13} + e_{23})\,;\,\varepsilon_0 e_{12}\}$, with $\varepsilon_0 = 0.01$ and with e_{11} to e_{12} being unit vectors in the deformation space. Note that we combined load states 13 and 23 for the fourth deformation state.

Next, for each sample the five independent components of the elasticity tensor $\boldsymbol{C}$ (see Eq. 2) are estimated by minimizing the L2-norm of $\sigma - \boldsymbol{C}^{\text{FEM}} : \varepsilon = 0$, where σ and ε are the stress and deformation states from the simulations. The specific choice of load states naturally implies different weights for the elasticity components during the least square optimization, as, for instance, the C_{33}^{FEM} is only involved in the e_{33} load state. This optimization strategy ensures the resulting elasticity tensor is transverse isotropic and incompressible. It also ensures that the components are consistently estimated through the several load states in which they play a role in.

To assess whether we fulfill the representative volume element (RVE) criterion, we employed the estimate of Wautier et al. (2015), which is based on correlation functions. RVE convergence is deemed to be satisfied when the ratio of linear sample size L (given in Table 1) and the correlation length l ($\sqrt[3]{l_x\, l_y\, l_z}$) exceeds 30. From this, we deduce that 92% of our samples fulfill this requirement, while 8% of the samples do not fulfill it. The latter samples have ice volume fractions ranging from 0.11 to 0.66.

3.5 Reparametrization of existing models

From the simulations we also reparametrize existing models from Sec. 2. The unknown parameters in the Gerling model (a_{ij} and b_{ij}), Zysset-Curnier model ($\lambda, \lambda', \mu, k$ and l) and the present model (ξ and β) are obtained by performing least squares regression on the simulated elasticity tensor components against the models from Sect. 2.2. The free parameters of all models were adjusted using a log-transformation of the elasticity tensor component, as done in Srivastava et al. (2016) or Zysset (2003).

4 Results

4.1 Present study parameterization

Figure 2 shows an overview of all results by plotting the simulated elasticity components C_{ij}^{FEM} (different rows) against ice volume fraction (column 1), the HS upper bound (column 2) and the normalized representation from Eq. (11). In the first top row (Fig. 2(a)-(c)), all elasticity components from all the samples are represented with different colors depending on the component of the elasticity tensor. In contrast, in the rest of the rows, only one component is represented at a time and the colors and symbols highlight the different samples, as defined in Table 1. The figure shows that the scatter of the simulated elasticity tensor components (C_{ij}^{FEM}) is maximal when plotted as a function of the ice volume fraction ϕ (left column), and that this scatter is reduced when plotted as a function of the HS upper bound C_{ij}^{U} instead (middle column).

Next, we use the improved correlation between C_{ij}^{FEM} and C_{ij}^{U} to derive the parameterization for each component according to Eq. (11), shown as the black curves (right column). Note that the non-linear transition behavior from the power law increases at low densities when approaching the value of ice is well captured for all the components. The performance, however, slightly differs for individual tensor components and is the best for C_{33}. We also stress that the data collapse for all tensor components in the normalized plot indicates that only two parameters are sufficient to obtain a decent picture of elasticity from Eq. (12).
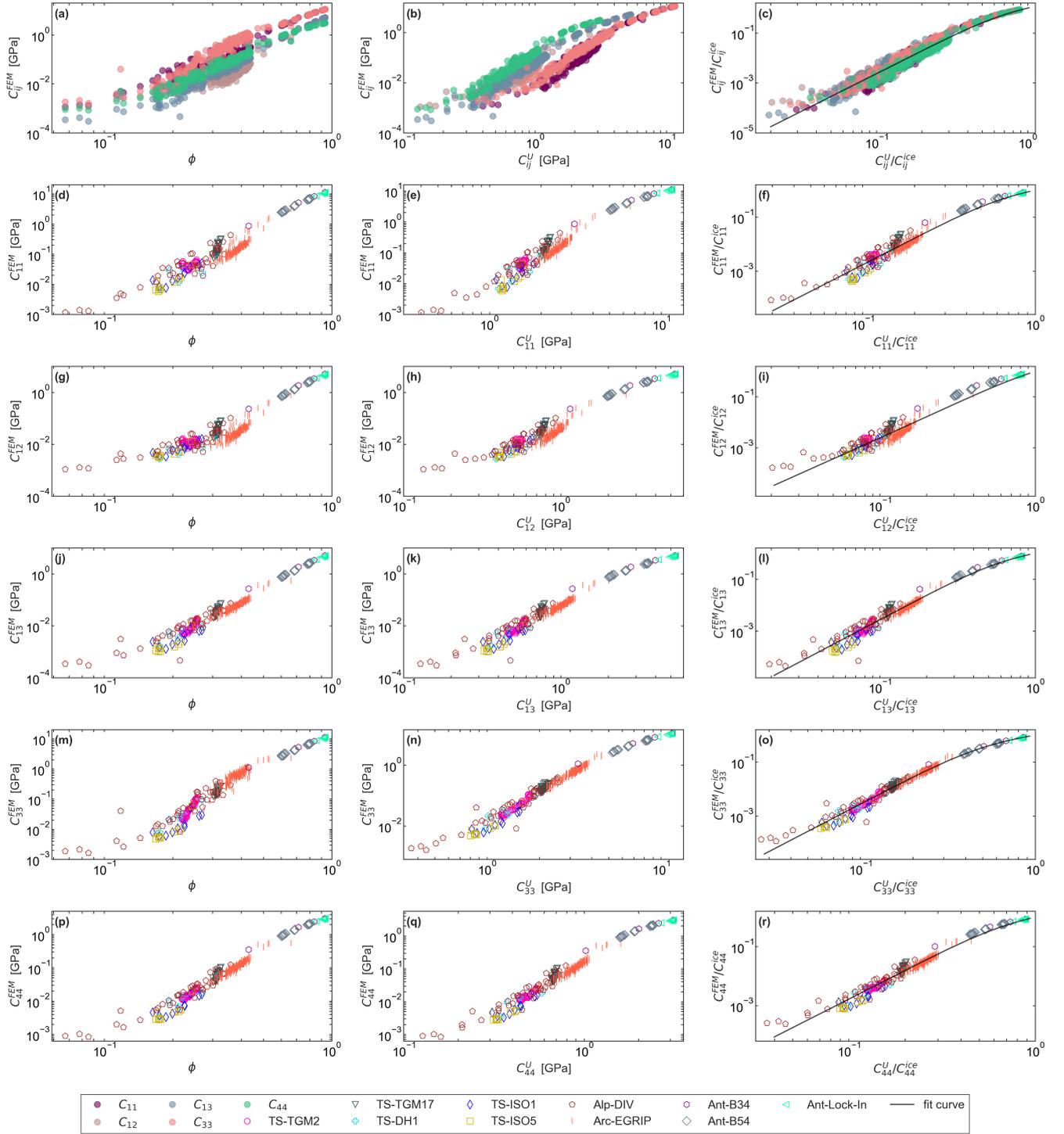
Figure 2. Simulated elasticity components C_{ij}^{FEM} (different rows) are shown as a function of volume fraction ϕ (left column), as a function of HS upper bound C_{ij}^{U} (middle column) and in the normalized version $C_{ij}^{\mathrm{U}}/C_{ij}^{\mathrm{ice}}$ (right column). The black curve represents the parameterization derived for all the components (2 parameters each). In the top row, the color scheme represents the components of the elasticity tensor. In the other rows, the colors and symbols represent the different samples considered in the present study, presented in Table 1.

4.2 Comparison to previous parameterizations

To examine the performance of the parameterization derived by fitting either individual components (see Fig. 3 top row) or fitting all the components of elastic modulus simultaneously (see Fig. 3 bottom row), we show a scatter plot of the C_{33} component of the elastic modulus evaluated from numerical simulations vs. the three parameterizations: density-based from Gerling (left), Zysset-Curnier (middle) and the present study parameterization (right). As with Fig. 2, the colors and symbols in the top row of Fig. 3 represent the different samples, while the colors in the bottom row represent the components of the elasticity tensor. A detailed overview of the parameters obtained for different parameterization and their coefficient of regression is given in Table 2. Note that these parameters differ from the values obtained in the original publication as the models were re-adjusted to fit our FEM simulations as explained in Sec. 3.5.
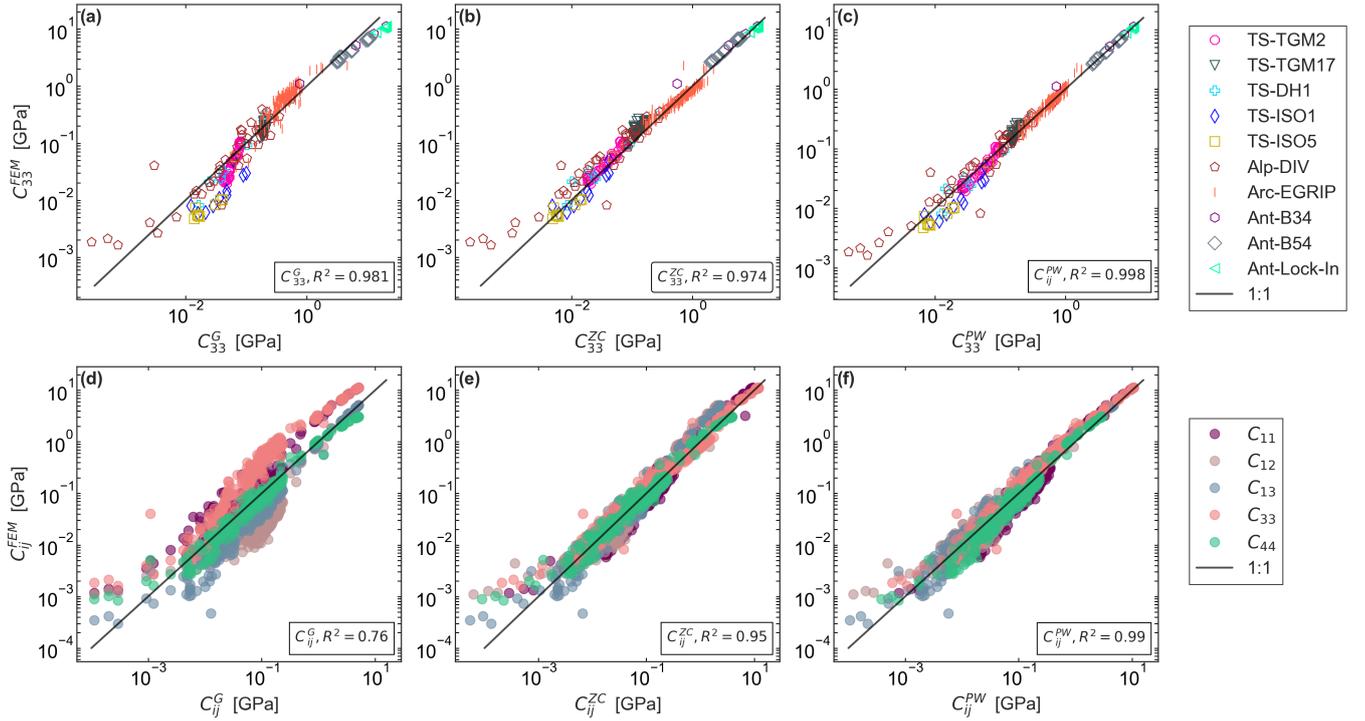
Figure 3. Comparison of simulated elastic modulus (C_{33}^{FEM}) to the Gerling et al. (2017) (G) density-based power law model given by Eq. (4), Zysset-Curnier (ZC) model Srivastava et al. (2016) given by Eq. (8) and present work parameterization (PW) given by Eq. (12) (from left to right). The given R^2 values correspond to the performance of the parameterization by fitting individual (top) or all components (bottom), respectively. In the top row, the colors and symbols represent the different samples considered in the present study, presented in Table 1. In the bottom row, the color scheme represents the components of the elasticity tensor.

Table 2. Parameters and regression coefficient obtained from least-square regression of the simulated elastic modulus employing different models on the entire data set.

Isotropic parameterization fitted for all components Gerling et al. (2017) - Eq. (4)	a_{ij}	b_{ij}	R^2
C_{ij}^{G}	6.73	4.08	0.76

Isotropic parameterization fitted for each component (Gerling et al., 2017) - Eq. (4)	a_{ij}	b_{ij}	R^2
C_{11}^{G}	9.51	3.93	0.992
C_{12}^{G}	2.13	3.85	0.994
C_{13}^{G}	5.31	4.46	0.997
C_{33}^{G}	27.33	4.26	0.980
C_{44}^{G}	4.70	3.88	0.978

Zysset-Curnier parameterization (Srivastava et al., 2016) - Eq. (8)	λ	λ'	μ
C_{ij}^{ZC}	0.56	0.19	0.16
	k	l	R^2
C_{ij}^{ZC}	4.02	-1.23	0.950

the present study parameterization fitted for all components - Eq. (12)	β	ξ	R^2
C_{ij}^{PW}	2.99	0.466	0.990

the present study parameterization fitted for individual components - Eq. (12)	β	ξ	R^2
C_{11}^{PW}	3.21	0.39	0.991
C_{12}^{PW}	2.69	0.90	0.976
C_{13}^{PW}	3.11	0.30	0.996
C_{33}^{PW}	3.32	0.18	0.998
C_{44}^{PW}	3.15	0.47	0.991

4.3 Comparison at high ice volume fractions

The improvement of the prediction of the elastic modulus using the present work parameterization C_{33}^{PW} at high-volume fraction is compared with elastic modulus determined by Kohnen (1972) formula given in Eq. 5, where the P-wave velocity of ice $v_{\mathrm{p}}^{\mathrm{ice}}$ is once calculated by using geometrical elastic modulus of ice ($v_{\mathrm{p}}^{\mathrm{ice}} = (C_{33}^{\mathrm{ice}}/\rho^{ice})^{0.5}$) and with the literature P-wave velocity of ice $v_{\mathrm{p}}^{\mathrm{ice}} \approx 3900\,\mathrm{ms}^{-1}$, that was notably estimated through vertical seismic profiling in Antarctica (Diez, 2013). This comparison is depicted in Fig. 4. We see that C_{33}^{KOH} based on the elastic modulus of ice used in this work exactly approaches the correct

limit, and is in line with our parameterization C_{33}^{PW} and the limit of elastic modulus for bubbly ice C_{33}^{DDS}. This validity of the C_{33}^{PW}, C_{33}^{KOH}, and C_{33}^{DDS} parametrization at high density is also confirmed by their agreement with the simulated C_{33}^{FEM} values.
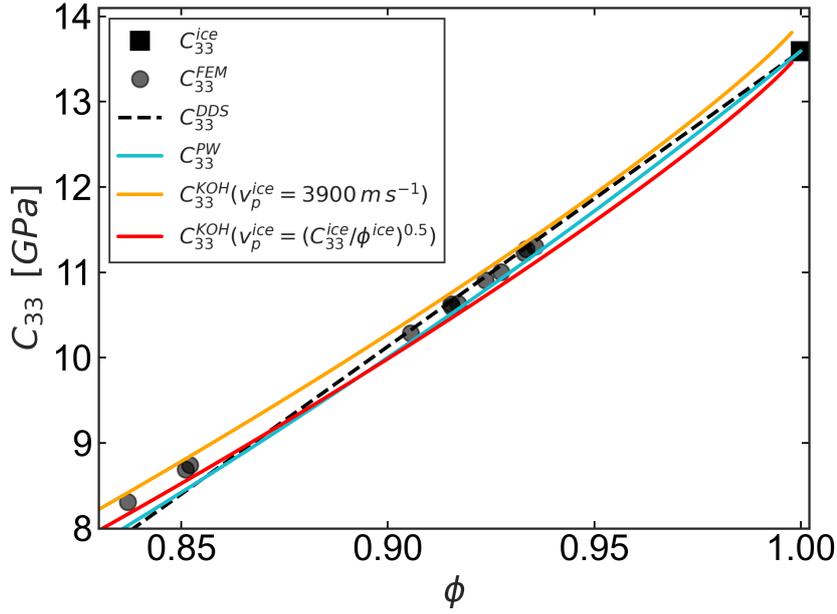
Figure 4. Comparison of present work parameterization C_{33}^{PW} with elastic modulus C_{33}^{KOH} determined by Kohnen (1972) empirical formula based on P-wave velocity and density (P-wave velocity is determined from structural elastic modulus of ice), elastictiy modulus C_{33}^{KOH} obtained by taking P-wave velocity as 3900 ms^{-1}, and with upper bound of elastic modulus for dilute dispersion (C_{33}^{DDS}). The black square represents the elastic modulus of ice (C_{33}^{ice}). The black dots correspond to simulations in this density regime (C_{33}^{FEM}).

4.4 Relative influence of geometrical anisotropy and density

305   While elasticity of snow, firn, and ice is predominantly controlled by density, we can now quantify the additional controls of geometrical anisotropy. To assess the distribution of geometrical anisotropy of the entire data set, we plot structural anisotropy parameter $\alpha = \ell_z / \ell_{xy}$ for all 391 microstructures as a function of ice volume fraction in Fig. 5(a). The highest anisotropy parameter ($\alpha = 1.87, \phi = 0.39$) is registered by an Arc-EGRIP sample.

     The potential error induced by assuming isotropy ($\alpha = 1$) in determining parameterization of elastic modulus is shown in 310   an error plot in Fig. 5 (b). Here, the error ($C_{33}^{\text{PW}}(\phi, \alpha) - C_{33}^{\text{PW}}(\phi, 1)/C_{33}^{\text{PW}}(\phi, 1)$ is shown as a two-dimensional contour plot as a function of ice volume fraction and the anisotropy parameter α. The relative error gives the percentage error induced between the elastic modulus computed as a function of anisotropy and as a function of isotropy, with zero relative error for isotropic structures. Fig. 5 presents the slice view of the microstructure for three different cases of α ($\alpha > 1$, $\alpha = 1$, and $\alpha < 1$). Note the vertical($\alpha > 1$) and horizontal($\alpha < 1$) geometrical orientation of the ice matrix.
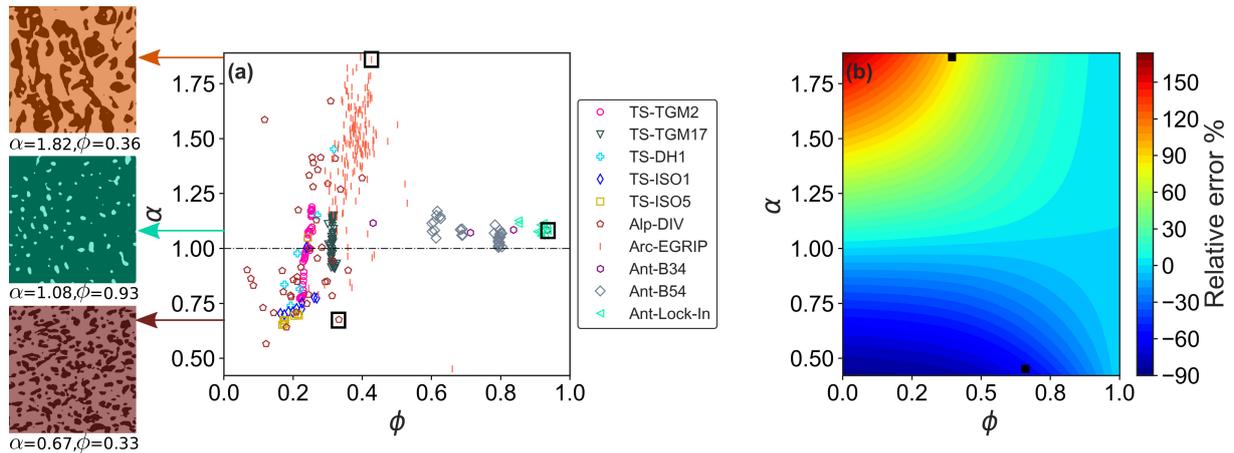
Figure 5. (a): Structural anisotropy of the microstructures (α) is plotted as a function of volume fraction ϕ. Isotropy is represented by dashed line for $\alpha = 1$. Three square boxes represent the three different geometrical anisotropic ratios $\alpha > 1$ (prolate inclusions), $\alpha = 1$ (isotropic), and $\alpha < 1$ (oblate inclusions) present in our data, for which a slice view of the microstructure in the yz plane is presented. (b): Contour plot showing $C_{33}^{\mathrm{PW}}(\phi, \alpha) - C_{33}^{\mathrm{PW}}(\phi, 1)/C_{33}^{\mathrm{PW}}(\phi, 1)$ as a function of anisotropy and volume fraction. The two black squares represents the relative error at the maximum and minimum anisotropy ratio $\alpha = 1.87$ and $\alpha = 0.45$ which occur in the present data set in (a). The color-bar represents the percentage of relative error computed for different geometrical anisotropic microstructures considered. Table 1 provides the description of the samples.

Figure 5 shows that the structural anisotropy α is an important component of the parametrization proposed in this work. However, as it is not straight-forward to measure the structural anisotropy and as elastic is highly sensitive to density, one may wonder how the errors induced by neglecting anisotropy compare to typical errors due to uncertainties on the density measurement. To answer this question, we compared the impact of neglecting anisotropy (that is to say assuming $\alpha = 1$) to that of a typical 5% uncertainty when measuring density using μCT (Proksch et al., 2015; Hagenmuller et al., 2016). Concretely, we applied our parametrization of the C_{33} component to three cases: case (a) corresponds to the ideal case of taking into account geometrical anisotropy ($\alpha \neq 1$) and assuming no uncertainty on density, case (b) corresponds to a case where geometrical anisotropy is accounted for ($\alpha \neq 1$) but with a 5% uncertainty on density, and case (c) corresponds to the case where geometrical anisotropy is neglected ($\alpha = 1$) but without density uncertainty. These three cases are applied to the Arc-EGRIP samples ($0.45 < \alpha < 1.87$ and $0.24 < \phi < 0.66$), which underwent TGM under natural conditions, and to the TS-TGM17 samples ($0.9 < \alpha < 1.15$ and $0.30 < \phi < 0.32$), which in contrast underwent TGM in controlled conditions. They are visible in Fig. 6 alongside estimation of the C_{33} component directly derived from the FE simulations, which serves as a reference. Neglecting anisotropy (case 3) leads to average errors of 39.8% and 21.7% for the Arc-EGRIP and TS-TGM17 samples, respectively. A 5% percent error on density, while taking into account anisotropy (case 2), yields average errors of 23% and 11.96% for the Arc-EGRIP and TS-TGM17 samples, respectively. This is to be compared with average errors of 14.56% and 11.96% when anisotropy is considered and when there is no error on density.
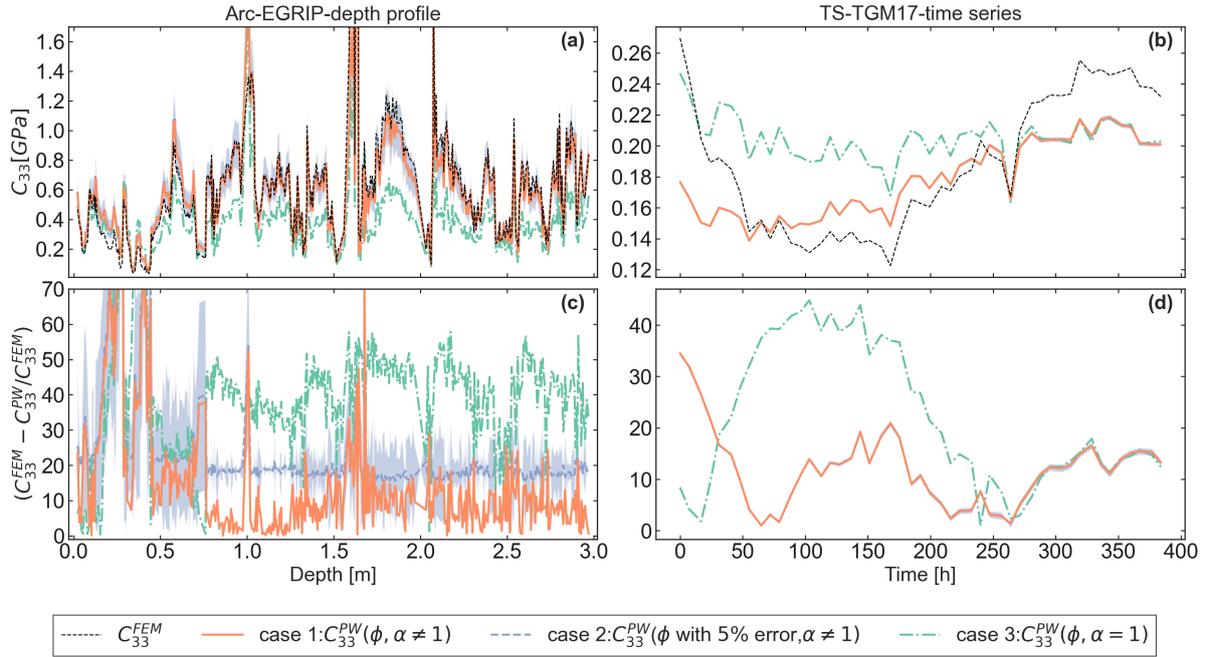
Figure 6. Comparison of elastic modulus calculated from FE simulations C_{33}^{FEM} to present work parameterization C_{33}^{PW} for (a) Arc-EGRIP samples as a function of depth and (b) for one of the TGM time series (TS-TGM17). C_{33}^{PW} is computed for the following three cases. Case 1: Accounting anisotropy without uncertainty on density $C_{33}^{\text{PW}}(\phi, \alpha \neq 1)$, case 2: Accounting anisotropy with 5% uncertainty on ϕ $C_{33}^{\text{PW}}(\phi$ with 5% error $,\alpha \neq 1)$, and case 3: not accounting for anisotropy without uncertainty on density $C_{33}^{\text{PW}}(\phi, \alpha = 1)$. Panels (c) and (d) show the norm of the relative errors of the three cases compared to the FE results. The shaded area for case 2 represents the spread resulting from a 5% variation in density.

4.5 Comparison of geometrical and crystallographic anisotropy

To assess the geometrical anisotropy in reference to the crystallographic anisotropy when determining the elastic properties of snow, firn, and ice for given ice volume fraction, we plot the geometrical Thomsen parameter ϵ_{geom}, obtained from Eq. 3, against ϕ in Fig. 7. For comparison, we also show the maximum crystallographic anisotropy that can be theoretically obtained, which is the known value of mono-crystalline ice at zero porosity ($\phi = 1$) given by $\epsilon_{\text{cryst}} = -0.0356$ (Petrenko and Whitworth, 1999a). The expected (but unknown) decay of ϵ_{cryst} for $\phi < 1$ is shown as a schematic (cf. discussion).
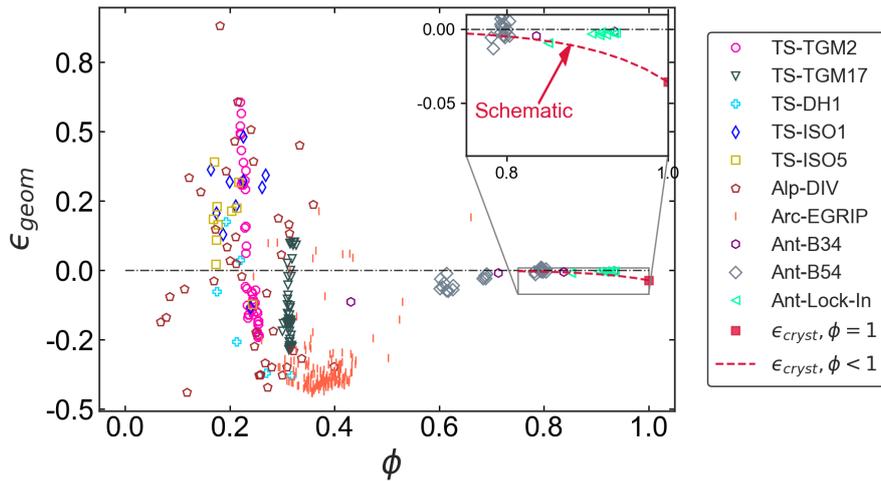
Figure 7. Geometrical and crystallographic Thomsen parameter, ϵ_{geom} and ϵ_{cryst}, plotted as a function of volume fraction ϕ to show the predominant influence of anisotropy (geometrical and crystallographical) on elastic properties. The red dashed line illustrates a schematic representation of the expected behavior of crystallographic anisotropy ϵ_{cryst} for $\phi < 1$. Sample name descriptions are given in Table 1.

5   Discussion

5.1   Summary of main results

The proposed empirical parameterization offers a crucial advantage by being applicable across the range of natural ice volume fractions, enabling accurate predictions of the effective elastic modulus (see Fig. 3). This broad range of applicability is supported by the fact that some of the temperature-gradient experiment samples used in this study have been independently compared with natural Arctic snow in terms of geometrical anisotropy (Leinss et al., 2020). Furthermore, these anisotropic samples fall into the intermediate density range ($250 \, \mathrm{kg/m^{-3}}$ to $500 \, \mathrm{kg/m^{-3}}$), where geometrical anisotropy exerts a substantial influence, in contrast with the lesser dominance of structural anisotropy at low and high densities. Therefore, we expect that our parameterization is sufficiently generic to capture typical anisotropic structures in snow. Furthermore, the samples used to derive the parametrization are diverse regarding their conditions of formation. Consequently, we expect this parameterization to yield reasonably accurate predictions of elastic properties for the whole range of natural porous snow, firn, and ice formations.

Previous parametrizations of the elastic modulus, based either on density alone (Eq. (4), Gerling et al. (2017)) or on density and anisotropy (Eq. (8), (Srivastava et al., 2016)), can significantly overestimate the elastic modulus when applied outside their validity range (see Fig. 1). The advantage of HS bound (Eq. (9)) is that it complies with the limiting behavior of bubbly ice (see Sec. 2.6) and does not overestimate the elastic properties as it approaches high volume fraction and incorporates the anisotropy (see Fig. 1). For constructing the empirical parameterization we exploited the fact that the elastic modulus should asymptotically tend to the behavior of randomly diluted spheres, reflecting the fact that low-porosity ice from ice cores mainly consist of convex (sphere like) air cavities (Fourteau et al., 2019). The validity of this assumption is reflected by Fig. 4,

which shows that numerical simulations coincide very well with the theoretical prediction of elasticity for dilute dispersions of spherical cavities (see Eq. (6)).

The relatively moderate change in the regression coefficient of our C_{33}^{PW} in comparison to previous parameterization C_{33}^{G} and C_{33}^{PW} (see Fig.3) reflects that anisotropy only has a sub-dominant influence on elasticity, while density remains the main param-
eter. However, capturing these sub-dominant influences may be very important for advanced microstructure characterization by alternative means, such as capturing macroscopic physical properties remotely (Leinss et al., 2016). Moreover, as shown is Section 4.4, neglecting anisotropy is the main source of error when estimating the elastic properties of a sample whose density has been measured with state-of-the-art techniques (Proksch et al., 2015; Hagenmuller et al., 2016).

Our parametrization of the elastic modulus is a good alternative to computationally expensive FE methods. Although other theoretical approximations, such as the self-consistent (SC) approximation, were previously employed by Wautier et al. (2015) to predict the effective elastic properties and by Calonne et al. (2019) to predict the effective thermal conductivity for the entire range of densities. SC approximations are based on implicit equations that need to be solved (Torquato, 2002a). Torquato (1998) showed that the SC give inadequate approximation of effective moduli of dispersions and overestimates the effective moduli in comparison to rigorous bounds. In contrast, the limiting behavior of the Hashin-Shtrikman bounds can provide an explicit formula for effective moduli.

It is notable that the range of elastic modulus varies for each tensor component (see Fig.2 (b)) plotted as a function of Hashin-Shtrikman bound. Hence, we parameterize elastic modulus for each component shown in Fig. 2 (column 3), as described in Sect. 2.6 using Eq. (12) and the two parameters ξ and β for each component are given in Table 2. We also observed that all five components collapse onto a single curve when normalizing the simulated values by ice moduli ($C_{ij}^{\text{FEM}}/C_{ij}^{\text{ice}}$) and plotting them as a function of the normalized HS upper ($C_{ij}^{\text{U}}/C_{ij}^{\text{ice}}$). This helped in the prediction of all five components of the elastic modulus with only two parameters in contrast to five parameters given by Zysset-Curnier parameterization used in Srivastava et al. (2016) for an orthotropic elasticity tensor.

5.2 Choice of the geometrical fabric tensor

Srivastava et al. (2016) demonstrated that the choice of the fabric tensor does not affect the prediction of anisotropy. Hence, the MIL fabric tensor, employed by the Zysset-Curnier parameterization in Srivastava et al. (2016), was replaced here by symmetric depolarization tensor (orientation tensor) M^*. In this way, the current elasticity parametrization involves exactly the same microstructure parameter (ϕ, α) as previous permittivity or thermal conductivity parametrizations (Leinss et al., 2016; Löwe et al., 2013). Weng (1992) evaluated bounds using a similar depolarization tensor based on two-point correlation functions assuming ellipsoidal symmetry. Their results were consistent with those of the Hashin-Shtrikman bounds evaluated by Eshelby tensor.

We note that the choice of the fabric tensor though has an impact on the sign of the fit parameter (l) in the Zysset-Curnier parameterization, yielding a negative value here in contrast to Srivastava et al. (2016). This can be explained because our depolarization tensor M^* given by Eq. (15) yields zero eigenvalue in the vertical direction for a vertically oriented microstructure. In contrast, the MIL fabric tensor is represented by $\langle m_i \otimes m_j \rangle$, with a local director m_i and divided by it's trace. If the ori-

390   entation is in the m_i direction, then the corresponding eigenvalue in this direction is maximized. Therefore, the sign of the

l parameter is reversed. A limitation of the MIL fabric tensor is, however that it is not able to detect interfacial anisotropy: Odgaard (1997) evaluated a two-dimensional "Swiss cheese" microstructure where the MIL analysis predicted an isotropic geometry despite the obvious, anisotropic arrangement of the spheres. The result of the analysis was influenced by the isotropic interfaces between the phases. Similar results were also observed by Klatt et al. (2017), when MIL analysis was performed on a

395   Boolean model with aligned Reuleaux triangles, it resulted in circles. MIL determination based on standard line or intersection counting techniques to determine MIL are time-consuming and sensitive to noise (Moreno et al., 2012).

5.3   Performance of the parameterization

Overall, the parameterization used in the present work C_{33}^{PW}, given by Eq. 11-12, had excellent agreement ($R^2 = 0.99$) when fit to all components simultaneously with 2 parameters in comparison to previous parameterizations Srivastava et al. (2016)

400   (volume-fraction and fabric-dependent) and Gerling et al. (2017) (volume-fraction-dependent), which yielded the coefficient of determination $R^2 = 0.76$ and $R^2 = 0.952$, respectively (see Table 2 and Fig. 3). Figure. 3(d) shows that the Gerling et al. (2017) density-based parameterization yields the best prediction for the component C_{44} when derived by fitting all components. This is because the C_{44} component values lie in between the diagonal component values C_{11} and C_{33} (typically higher values) and off-diagonal component values C_{12} and C_{13} (typically lower values). The highest improvement over density based parametrizations

405   is achieved for the C_{33} component for the (TS-TGM2, TS-TGM17, and Arc-EGRIP) samples, which becomes apparent when plotted as a function of HS upper bound or volume fraction (see Fig. 2). All of these samples have an ice matrix predominantly oriented in z-direction (see Fig. 5 (a)) with the anisotropy ratio $\alpha > 1$. Such vertically oriented structures are generated by strong temperature gradient metamorphism (Calonne et al., 2012; Löwe et al., 2013; Leinss et al., 2020) occurring in the snow, firn, and ice. This is evident for temperature gradient time series (TS-TGM2 and TS-TGM17) from Fig. 5 (a), where we see

410   the change from a horizontal orientation of ice matrix into a vertical orientation. The improvement of the prediction of the elastic modulus mainly in z-direction is consistent with previously derived properties such as thermal conductivity for snow (see, Löwe et al., 2013). EastGRIP (Arc-EGRIP) samples extracted from the firn in Greenland also display similar kind of geometrical anisotropy in the vertical direction (Montagnat et al., 2020).

    To further test the performance of our parameterization, we considered data (ice volume fraction and correlation functions)

415   provided by Wautier et al. (2015). The data display values of α ranging from 0.65 to 1.26, and of ϕ ranging from 0.10 to 0.59. We applied our parameterization on these data using Eq. (12) and compared the obtained results to the elastic stiffness tensor computed from FE simulations of Wautier et al. (2015), Srivastava et al. (2016) and from the present work. We also added the other parameterizations derived from FE simulations (namely Köchle and Schneebeli, 2014; Gerling et al., 2017), with ϕ ranging from 0.10 to 0.59. We found that PW parameterization applied to the data of Wautier et al. (2015) differs from the

420   Wautier et al. (2015) simulation results. However, despite the scatter, both our FEM simulations and PW parameterization lie within the range of FE results from Srivastava et al. (2016), Köchle and Schneebeli (2014), and Gerling et al. (2017).

    Using the new parametrization, it is possible to assess the maximum error in the prediction of elasticity if anisotropy was not taken into account (see Fig. 5(b)). As the relative error is not the same for microstructures with vertical and horizontal

orientation of ice matrix (see Fig. 5(a)), the error plot is non-symmetric in α (see Fig. 5(b)). The relative error of the elastic

425   modulus for vertical ice matrix orientation (TS-TGM2, TS-TGM17 and Arc-EGRIP) ($\alpha > 1$) (see Fig. 5(b), top half) is larger than 100%. The relative error for horizontal orientation of ice matrix ($\alpha < 1$) seen for ϕ between snow to ice is up to -90%. From Fig. 5(a) and, 5(b), it is clear that for intermediate volume fractions in the range $0.3 < \phi < 0.5$, very different anisotropy values are possible for a similar density. Using the extreme values from Fig. 5(b) the prediction of elastic modulus solely as a function of ϕ could miss variations up to 200%. For $\phi \to 1$, the relative error must approach zero, since for vanishing porosity

430   (polycrystalline) ice becomes geometrically isotropic.

5.4   Comparison of geometrical and crystallographical anisotropy

In Fig. 5(a) and Fig. 7 we see the typical evolution of the geometrical anisotropy in snow, firn, and ice, with a sharp increase in geometrical anisotropy with density in low-density snow and its survival up to high densities. Initially, at low-density snow exhibits a horizontal orientation of ice matrix (Leinss et al., 2016). As the volume fraction increases from snow to

435   firn, we observe the transition of the orientation to the vertical direction. This change is a result of temperature gradient metamorphism, which can be easily confirmed from the temperature gradient metamorphism experiments (TS-TGM2 and TS-TGM17), and also from the Arc-EGRIP dataset (Leinss et al. (2020). The existence of geometric anisotropy in polar snow are well known (Fujita et al., 2014; Moser et al., 2020) and can be quantitatively related to temperature gradient metamorphism (Montagnat et al., 2020). When the volume fraction of ice increases further from firn to bubbly ice, the microstructures relax to

440   a geometrically isotropic state. This is a consequence of gravitational settling and densification of snow (Leinss et al., 2020). However, we infer from Fig. 5 (a) that the vertical geometrical anisotropy generated near the surface survives beyond the bubble close-off transition around $\phi \approx 0.92$ that underlies the Ant-Lock-In data, as discussed in Fourteau et al. (2019). This raises the question at which point exactly the crystallographic anisotropy will become the dominant type of anisotropy.

    To this end, we have quantified the geometrically elastic anisotropy by deriving the corresponding Thomsen parameter ϵ_{geom}

445   for the entire range of ice volume fraction (see Fig. 7). This clearly reveals that the geometrical anisotropy dominates snow and firn for ice volume fraction $\phi < 0.7$ in our data. For bubbly ice the situation is a bit more complicated. The crystallographic Thomsen parameter of ice $\epsilon_{\mathrm{cryst}}$ shown in Fig. 7 is only valid for $\phi = 1$, where the geometrical Thomsen parameter ϵ_{geom} must vanish. However, it can be expected that in the range $0.7 < \phi < 1$ the geometrical and crystallographic anisotropy are of similar magnitude since the crystallographic Thomsen parameter $\epsilon_{\mathrm{cryst}}$ must decay from its ice value when increasing the porosity. To

450   understand this phenomenon, one can assume a volume-filling monocrystal, with a Thomsen parameter $\epsilon_{\mathrm{cryst}}$ that corresponds the maximum possible crystallographic anisotropy. Now, if this volume is gradually filled with an isotropic inclusion of air, the anisotropic behavior of the hollowed mono-crystal decays. This behavior is shown as a schematic line in the inset of Fig. 7 and highlights the importance of consideration of both kinds of anisotropies for very high density. Such an influence of very low porosity on the crystallographic fabric is also implied by the results of (Hellmann et al., 2021).

455   For microstructures in the volume fraction range $0.7 < \phi < 1$, it may be thus important in the future to consider concurrent effects of crystallographical and geometrical anisotropy, which is presently nonexistent. It is important to know the dominant

anisotropy (geometrical or crystallographic) for a given volume fraction for the prediction of elastic properties. Previous studies mostly consider crystallographic anisotropy, which may, however, become dominant only very close to $\phi = 1$

5.5 Applicability of the current parameterization

460 To ease the applicability of the present parameterization, we provide the Python scripts with the data and the necessary functions to compute the parametrized elasticity tensor as a function of a sample's density and anisotropy and of the shear and bulk modulus of ice. Also, while the parameterization of the elasticity tensor was derived using the elastic properties of ice at $-16°$ C, one can directly transpose the parameterization to a different temperature. This is readily done by taking into account the temperature dependence of the ice elastic properties that appear in the parameterization. Finally, as the purely elastic behavior

465 of a porous material does not depend on grain size explicitly but only on its microstructural shape (as seen in the Eshelby tensor described in Appendix B), the proposed parameterization is applicable regardless of the grain size of the considered sample.

6 Conclusions

Using a transformation of the anisotropic Hashin-Shtrikman bounds, we derived a new closed-form parametrization for the effective elasticity tensor as a function of volume fraction and geometrical anisotropy applicable from fresh snow to bubbly ice.

470 Thereby, we extend the set of parameterizations of physical parameters with a similar focus on the full range of volume fractions (Calonne et al., 2019; Picard et al., 2022). We have demonstrated the advantages over previous elasticity parametrizations in view of performance and the correct asymptotic behavior for bubbly ice. Given the distribution of naturally occurring geometrical anisotropy, the uncertainty range of elastic moduli predictions is up to 200% for intermediate volume fractions of $0.3 < \phi < 0.5$ if only density was considered in the parametrization.

475 The new parametrization is a crucial tool for use in different applications in cryospheric sciences. In particular, we seek to trigger new microstructure retrievals through advanced anisotropic inversion methods of seismic data (Wu et al., 2022). Along these lines, our results shed new light on the relative importance of the two different types of elastic anisotropy (crystallographic, geometrical) in snow and firn that may influence the interpretation of seismic measurements (Schlegel et al., 2019). The geometrical anisotropy is clearly dominating the crystallographic anisotropy for $\phi < 0.7$, and must be taken into account

480 when discussing anisotropy in near surface seismics (Chaput et al., 2022). While the geometrical anisotropy quickly decays with depth, remainders still persists down to the close-off depth, and it remains to be investigated in the future how *concurrent* fabrics (geometrical and crystallographic) will elastically interact in bubbly ice.

Code and data availability. We published the data and the code of this study on the data portal EnviDat under the following site (https://www.doi.org/10.16904/envidat.462).

Appendix A: Isotropic elasticity tensor

Elasticity tensor in terms of bulk modulus K and shear modulus G for an isotropic case is given as

$$
C = \begin{bmatrix}
K+4G/3 & K-2G/3 & K-2G/3 & 0 & 0 & 0 \\
K-2G/3 & K+4G/3 & K-2G/3 & 0 & 0 & 0 \\
K-2G/3 & K-2G/3 & K+4G/3 & 0 & 0 & 0 \\
0 & 0 & 0 & G & 0 & 0 \\
0 & 0 & 0 & 0 & G & 0 \\
0 & 0 & 0 & 0 & 0 & G
\end{bmatrix}, \tag{A1}
$$

and Young's modulus $E = \dfrac{9KG}{3K+G}$ and Poisson's ratio $\nu = \dfrac{3K-2G}{2(3K+G)}$.

Appendix B: Eshelby tensor

490   The Eshelby tensor S is defined in terms of elliptical integrals. For the case of a spheroidal inclusion with semi-axis given in terms of correlations lengths $\ell_x = \ell_y = a$ and $\ell_z = b$, with symmetry axis aligned in z-direction embedded in a transverse isotropic comparison phase results in transverse isotropic Eshelby tensor and is defined in terms of with the components of S_{ijkl} given by (Torquato, 2002a; Parnell and Calvo-Jurado, 2015):

$$
S_{1111} = S_{2222} = \frac{3}{8(1-v_1)}\frac{\alpha^2}{\alpha^2-1} + \frac{1}{4(1-v_1)}\left[1 - 2v_1 - \frac{9}{4(\alpha^2-1)}\right]q,
$$

$$
S_{3333} = \frac{1}{2(1-v_1)}\left\{1 - 2v_1 + \frac{3\alpha^2-1}{\alpha^2-1} - \left[1 - 2v_1 + \frac{3\alpha^2}{\alpha^2-1}\right]q\right\},
$$

$$
S_{1122} = S_{2211} = \frac{1}{4(1-v_1)}\left\{\frac{\alpha^2}{2(\alpha-1)} - \left[1 - 2v_1 + \frac{3}{4(\alpha^2-1)}\right]q\right\},
$$

$$
S_{1133} = S_{2233} = \frac{1}{2(1-v_1)}\left\{\frac{-\alpha^2}{\alpha^2-1} + \frac{1}{2}\left[\frac{3\alpha^2}{\alpha^2-1} - (1-2v_1)\right]q\right\}, \tag{B1}
$$

$$
S_{3311} = S_{3322} = \frac{1}{2(1-v_1)}\left\{2v_1 - 1 - \frac{1}{\alpha^2-1} + \left[1 - 2v_1 + \frac{3}{2(\alpha^2-1)}\right]q\right\},
$$

$$
S_{1212} = \frac{1}{4(1-v_1)}\left\{\frac{\alpha^2}{2\alpha^2-1} + \left[1 - 2v_1 - \frac{3}{4(\alpha^2-1)}\right]q\right\},
$$

$$
S_{1313} = S_{2323} = \frac{1}{4(1-v_1)}\left\{1 - 2v_1 - \frac{\alpha^2+1}{\alpha^2-1} - \frac{1}{2}\left[1 - 2v_1 - \frac{3(\alpha^2+1)}{\alpha^2-1}\right]q\right\},
$$

with Poisson ratio of the comparison material given by v_1, α is the aspect ratio of spheroid given in terms of correlation lengths (ℓ_z/ℓ_{xy}) and q is defined by

$$q = \begin{cases} \dfrac{\alpha}{(\alpha^2 - 1)^{3/2}}[\alpha(\alpha^2 - 1)^{1/2} - \cosh^{-1}\alpha], \ \alpha \geq 1, \\ \dfrac{\alpha}{(1 - \alpha^2)^{3/2}}[\cos^{-1}\alpha - \alpha(1 - \alpha^2)^{1/2}], \ \alpha \leq 1, \end{cases} \tag{B2}$$

Several limits of the Eshelby tensor for transverse isotropic materials can be derived. For ice matrix orientation with needle-shaped structures $(\alpha \to \infty, q = 1)$, the Eshelby tensor reads

$$S_{1111} = S_{2222} = \frac{5 - 4v_1}{8(1 - v_1)}, \ S_{3333} = 0$$

$$S_{1122} = S_{2211} = \frac{4v_1 - 1}{8(1 - v_1)}, \ S_{1133} = S_{2233} = \frac{v_1}{2(1 - v_1)}, \tag{B3}$$

$$S_{3311} = S_{3322} = 0, \ S_{1212} = \frac{3 - 4v_1}{8(1 - v_1)}, \ S_{1313} = S_{2323} = \frac{1}{4}.$$

For inclusion with disk-shaped structures $(\alpha = 0, q = 0)$, the components of Eshelby are then given by

$$S_{3333} = 1, \ S_{3311} = S_{3322} = \frac{v_1}{1 - v_1}, \ S_{1313} = S_{2323} = \frac{1}{2}. \tag{B4}$$

Appendix C: Definition of function $Q(\alpha)$

For the evaluation of the depolarization tensor M^* in Eq.15 the definition of function $Q(\alpha)$ is given as (Torquato, 2002a)

$$Q = \begin{cases} \dfrac{1}{2}\left\{1 + \dfrac{1}{\alpha^2 - 1}\left[1 - \dfrac{1}{2\chi_b(\alpha)}\ln\left(\dfrac{1 + \chi_b(\alpha)}{1 - \chi_b(\alpha)}\right)\right]\right\}, \alpha > 1, \\ \dfrac{1}{2}\left\{1 + \dfrac{1}{\alpha^2 - 1}\left[1 - \dfrac{1}{\chi_b(\alpha)}\mathrm{atan}(\chi_a(\alpha))\right]\right\}, \alpha < 1, \end{cases} \tag{C1}$$

with $\chi_a(\alpha)^2 = -\chi_b(\alpha)^2 = 1/\alpha^2 - 1$. For the case, $\alpha = 1$, $Q = 1/3$.

Author contributions. KS conducted simulations, analyzed the data, created the figures and prepared the manuscript. JF collected the B34/54 data. KF prepared the Lock-in data and edited the manuscript. HL received the funding, supervised the study, and edited the manuscript.

Competing interests. The authors declare no competing interests.

Acknowledgements. We thank Pascal Hagenmuller, Antoine Wautier, Kris Houdyshell, and an anonymous reviewer for helpful comments that helped improve the manuscript. The Swiss National Science Foundation funded this study through grant no. 200020_178831.

References

Baker, I.: Microstructural characterization of snow, firn and ice, Philosophical Transactions of the Royal Society A: Mathematical, Physical and Engineering Sciences, 377, 20180 162, https://doi.org/10.1098/rsta.2018.0162, https://royalsocietypublishing.org/doi/abs/10.1098/rsta.2018.0162, 2019.

Bobillier, G., Bergfeld, B., Capelli, A., Dual, J., Gaume, J., van Herwijnen, A., and Schweizer, J.: Micromechanical modeling of snow failure, The Cryosphere, 14, 39–49, https://doi.org/10.5194/tc-14-39-2020, https://tc.copernicus.org/articles/14/39/2020/, 2020.

Calonne, N., Geindreau, C., Flin, F., Morin, S., Lesaffre, B., Roscoat, S. R. D., and Charrier, P.: 3-D image-based numerical computations of snow permeability: links to specific surface area, density, and microstructural anisotropy, The Cryosphere, 6, 939–951, 2012.

Calonne, N., Flin, F., Lesaffre, B., Dufour, A., Roulle, J., Puglièse, P., Philip, A., Lahoucine, F., Geindreau, C., Panel, J.-M., du Roscoat, S. R., and Charrier, P.: CellDyM: A room temperature operating cryogenic cell for the dynamic monitoring of snow metamorphism by time-lapse X-ray microtomography, Geophysical Research Letters, 42, 3911–3918, https://doi.org/https://doi.org/10.1002/2015GL063541, https://agupubs.onlinelibrary.wiley.com/doi/abs/10.1002/2015GL063541, 2015.

Calonne, N., Milliancourt, L., Burr, A., Philip, A., Martin, C. L., Flin, F., and Geindreau, C.: Thermal Conductivity of Snow, Firn, and Porous Ice From 3-D Image-Based Computations, Geophysical Research Letters, 46, 13 079–13 089, https://doi.org/https://doi.org/10.1029/2019GL085228, https://agupubs.onlinelibrary.wiley.com/doi/abs/10.1029/2019GL085228, 2019.

Chaput, J., Aster, R., Karplus, M., and Nakata, N.: Ambient high-frequency seismic surface waves in the firn column of central west Antarctica, Journal of Glaciology, 68, 785–798, https://doi.org/10.1017/jog.2021.135, 2022.

Cowin, S. C.: The relationship between the elasticity tensor and the fabric tensor, Mechanics of Materials, 4, 137 – 147, https://doi.org/https://doi.org/10.1016/0167-6636(85)90012-2, http://www.sciencedirect.com/science/article/pii/0167663685900122, 1985.

Diez, A.: Effects of cold glacier ice crystal anisotropy on seismic data, Ph.D. thesis, http://digbib.ubka.uni-karlsruhe.de/volltexte/1000037984, 2013.

Diez, A. and Eisen, O.: Seismic wave propagation in anisotropic ice - Part 1: Elasticity tensor and derived quantities from ice-core properties, The Cryosphere, 9, 367–384, https://doi.org/10.5194/tc-9-367-2015, http://www.the-cryosphere.net/9/367/2015/, 2015.

Diez, A., Eisen, O., Hofstede, C., Lambrecht, A., Mayer, C., Miller, H., Steinhage, D., Binder, T., and Weikusat, I.: Seismic wave propagation in anisotropic ice - Part 2: Effects of crystal anisotropy in geophysical data, The Cryosphere, 9, 385–398, https://doi.org/10.5194/tc-9-385-2015, 2015.

Eshelby, J. D. and Peierls, R. E.: The determination of the elastic field of an ellipsoidal inclusion, and related problems, Proceedings of the Royal Society of London. Series A. Mathematical and Physical Sciences, 241, 376–396, https://doi.org/10.1098/rspa.1957.0133, https://royalsocietypublishing.org/doi/abs/10.1098/rspa.1957.0133, 1957.

Fourteau, K., Martinerie, i., Faïn, X., Schaller, C. F., Tuckwell, R. J., Löwe, H., Arnaud, L., Magand, O., Thomas, E. R., Freitag, J., Mulvaney, R., Schneebeli, M., and Lipenkov, V. Y.: Multi-tracer study of gas trapping in an East Antarctic ice core, Cryosphere, 13, 3383–3403, https://doi.org/10.5194/tc-13-3383-2019, 2019.

Freitag, J., Wilhelms, F., and Kipfstuhl, S.: Microstructure-dependent densification of polar firn derived from X-ray microtomography, Journal of Glaciology, 50, 243–250, https://doi.org/10.3189/172756504781830123, 2004.

Frolov, A. D. and Fedyukin, I. V.: Elastic properties of snow-ice formations in their whole density range, Annals of Glaciology, 26, 55–58, https://doi.org/10.3189/1998AoG26-1-55-58, 1998.

Fujita, S., Hirabayashi, M., Goto-Azuma, K., Dallmayr, R., Satow, K., Zheng, J., and Dahl-Jensen, D.: Densification of layered firn of the
ice sheet at NEEM, Greenland, Journal of Glaciology, 60, 905–921, https://doi.org/10.3189/2014JoG14J006, 2014.

Garboczi, E. J.: Finite element and finite difference programs for computing the linear electrical and elastic properties of digital images of
random material,NISTIR 6269, US Department of Commerce, 1998.

Gaume, J., Chambon, G., Eckert, N., and Naaim, M.: Influence of weak-layer heterogeneity on snow slab avalanche release: application to
the evaluation of avalanche release depths, Journal of Glaciology, 59, 423–437, https://doi.org/10.3189/2013JoG12J161, 2013.

Gerling, B., Löwe, H., and van Herwijnen, A.: Measuring the Elastic Modulus of Snow, Geophysical Research Letters, 44, 11,088–11,096,
https://doi.org/https://doi.org/10.1002/2017GL075110, https://agupubs.onlinelibrary.wiley.com/doi/abs/10.1002/2017GL075110, 2017.

Hagenmuller, P., Matzl, M., Chambon, G., and Schneebeli, M.: Sensitivity of snow density and specific surface area measured
by microtomography to different image processing algorithms, The Cryosphere, 10, 1039–1054, https://doi.org/10.5194/tc-10-1039-2016,
https://tc.copernicus.org/articles/10/1039/2016/, 2016.

Hashin, Z.: Theory of mechanical behavior of heterogeneous media, 1963.

Hashin, Z. and Shtrikman, S.: On some variational principles in anisotropic and nonhomogeneous elasticity, Journal of the Mechanics and
Physics of Solids, 10, 335 – 342, https://doi.org/https://doi.org/10.1016/0022-5096(62)90004-2, http://www.sciencedirect.com/science/
article/pii/0022509662900042, 1962.

Hellmann, S., Grab, M., Kerch, J., Löwe, H., Bauder, A., Weikusat, I., and Maurer, H.: Acoustic velocity measurements for detecting
the crystal orientation fabrics of a temperate ice core, The Cryosphere, 15, 3507–3521, https://doi.org/10.5194/tc-15-3507-2021, https:
//tc.copernicus.org/articles/15/3507/2021/, 2021.

Hill, R.: Elastic properties of reinforced solids: Some theoretical principles, Journal of the Mechanics and Physics of
Solids, 11, 357 – 372, https://doi.org/https://doi.org/10.1016/0022-5096(63)90036-X, http://www.sciencedirect.com/science/article/pii/
002250966390036X, 1963.

Ishimoto, H., Adachi, S., Yamaguchi, S., Tanikawa, T., Aoki, T., and Masuda, K.: Snow particles extracted from X-ray computed micro-
tomography imagery and their single-scattering properties, Journal of Quantitative Spectroscopy and Radiative Transfer, 209, 113–128,
https://doi.org/https://doi.org/10.1016/j.jqsrt.2018.01.021, https://www.sciencedirect.com/science/article/pii/S002240731730657X, 2018.

Klatt, M. A., Schröder-Turk, G. E., and Mecke, K.: Mean-intercept anisotropy analysis of porous media. II. Conceptual
shortcomings of the MIL tensor definition and Minkowski tensors as an alternative, Medical Physics, 44, 3663–3675,
https://doi.org/https://doi.org/10.1002/mp.12280, https://aapm.onlinelibrary.wiley.com/doi/abs/10.1002/mp.12280, 2017.

Kohnen, H.: Über die Beziehung zwischen seismischen Geschwindigkeiten und der Dichte in Firn und Eis, Zeitschrift für Geophysik. 38(5).
Germany, 38, 925, 1972.

Krol, Q. and Loewe, H.: Relating optical and microwave grain metrics of snow: the relevance of grain shape, The Cryosphere, 10, 2847–2863,
2016.

Köchle, B. and Schneebeli, M.: Three-dimensional microstructure and numerical calculation of elastic properties of alpine snow with a focus
on weak layers, Journal of Glaciology, 60, 705–713, https://doi.org/10.3189/2014JoG13J220, 2014.

Leinss, S., Löwe, H., Proksch, M., Lemmetyinen, J., Wiesmann, A., and Hajnsek, I.: Anisotropy of seasonal snow measured by polarimetric
phase differences in radar time series, The Cryosphere, 10, 1771 – 1797, https://doi.org/10.3929/ethz-b-000121191, 2016.

Leinss, S., Löwe, H., Proksch, M., and Kontu, A.: Modeling the evolution of the structural anisotropy of snow, Cryosphere, 14, 51–75,
https://doi.org/10.5194/tc-14-51-2020, 2020.

Löwe, H., Riche, F., and Schneebeli, M.: A general treatment of snow microstructure exemplified by an improved relation for thermal conductivity, The Cryosphere, 7, 1473–1480, https://doi.org/10.5194/tc-7-1473-2013, https://tc.copernicus.org/articles/7/1473/2013/, 2013.

Montagnat, M., Azuma, N., Dahl-Jensen, D., Eichler, J., Fujita, S., Gillet-Chaulet, F., Kipfstuhl, S., Samyn, D., Svensson, A., and Weikusat, I.: Fabric along the NEEM ice core, Greenland, and its comparison with GRIP and NGRIP ice cores, The Cryosphere, 8, 1129–1138, https://doi.org/10.5194/tc-8-1129-2014, https://tc.copernicus.org/articles/8/1129/2014/, 2014.

Montagnat, M., Löwe, H., Calonne, N., Schneebeli, M., Matzl, M., and Jaggi, M.: On the Birth of Structural and Crystallographic Fabric Signals in Polar Snow: A Case Study From the EastGRIP Snowpack, Frontiers in Earth Science, 8, 365, https://doi.org/10.3389/feart.2020.00365, 2020.

Moreno, R., Borga, M., and Smedby, Ö.: Generalizing the mean intercept length tensor for gray-level images, Medical Physics, 39, 4599–4612, https://doi.org/https://doi.org/10.1118/1.4730502, https://aapm.onlinelibrary.wiley.com/doi/abs/10.1118/1.4730502, 2012.

Moreno, R., Smedby, Ö., and Pahr, D.: Prediction of apparent trabecular bone stiffness through fourth-order fabric tensors, Biomechanics and Modeling in Mechanobiology, 15, 831–844, 2016.

Moser, D. E., Hörhold, M., Kipfstuhl, S., and Freitag, J.: Microstructure of Snow and Its Link to Trace Elements and Isotopic Composition at Kohnen Station, Dronning Maud Land, Antarctica, Frontiers in Earth Science, 8, https://doi.org/10.3389/feart.2020.00023, https://www.frontiersin.org/articles/10.3389/feart.2020.00023, 2020.

Nemat-Nasser, S. and Hori, M.: Universal Bounds for Overall Properties of Linear and Nonlinear Heterogeneous Solids, Journal of Engineering Materials and Technology, 117, 412–432, https://doi.org/10.1115/1.2804735, https://doi.org/10.1115/1.2804735, 1995.

Odgaard, A.: Three-dimensional methods for quantification of cancellous bone architecture, Bone, 20, 315–328, https://doi.org/10.1016/S8756-3282(97)00007-0, 1997.

Parnell, W. and Calvo-Jurado, C.: On the computation of the Hashin-Shtrikman bounds for transversely isotropic two-phase linear elastic fibre-reinforced composites, Journal of Engineering Mathematics, https://doi.org/doi:10.1107/s10665-014-9777-3, 2015.

Petrenko, V. and Whitworth, R.: Physics of Ice, OUP Oxford, https://books.google.ch/books?id=oC941a8lXWIC, 1999a.

Petrenko, V. F. and Whitworth, R. W.: Physics of ice, OUP Oxford, 1999b.

Picard, G., Löwe, H., and Mätzler, C.: Brief communication: A continuous formulation of microwave scattering from fresh snow to bubbly ice from first principles, The Cryosphere, 16, 3861–3866, https://doi.org/10.5194/tc-16-3861-2022, https://tc.copernicus.org/articles/16/3861/2022/, 2022.

Proksch, M., Löwe, H., and Schneebeli, M.: Density, specific surface area, and correlation length of snow measured by high-resolution penetrometry, Journal of Geophysical Research: Earth Surface, 120, 346–362, https://doi.org/https://doi.org/10.1002/2014JF003266, https://agupubs.onlinelibrary.wiley.com/doi/abs/10.1002/2014JF003266, 2015.

Roberts, A. P. and Garboczi, E. J.: Computation of the linear elastic properties of random porous materials with a wide variety of microstructure, Proceedings of the Royal Society A: Mathematical, Physical and Engineering Sciences, 458, 1033–1054, https://doi.org/10.1098/rspa.2001.0900, 2002.

Salomon, M. L., Maus, S., and Petrich, C.: Microstructure evolution of young sea ice from a Svalbard fjord using micro-CT analysis, Journal of Glaciology, 68, 571–590, https://doi.org/10.1017/jog.2021.119, 2022.

Saruya, T., Fujita, S., Iizuka, Y., Miyamoto, A., Ohno, H., Hori, A., Shigeyama, W., Hirabayashi, M., and Goto-Azuma, K.: Development of crystal orientation fabric in the Dome Fuji ice core in East Antarctica: implications for the deformation regime in ice sheets, The Cryosphere, 16, 2985–3003, https://doi.org/10.5194/tc-16-2985-2022, https://tc.copernicus.org/articles/16/2985/2022/, 2022.

Scapozza, C.: Entwicklung eines dichte- und temperaturabhängigen Stoffgesetzes zur Beschreibung des visko-elastischen Verhaltens von Schnee, Ph.D. thesis, ETH Zurich, Zürich, https://doi.org/10.3929/ethz-a-004680249, diss., Technische Wissenschaften, Eidgenössische Technische Hochschule ETH Zürich, Nr. 15357, 2004., 2004.

Schlegel, R., Diez, A., Löwe, H., Mayer, C., Lambrecht, A., Freitag, J., Miller, H., Hofstede, C., and Eisen, O.: Comparison of elastic moduli from seismic diving-wave and ice-core microstructure analysis in Antarctic polar firn, Annals of Glaciology, 60, 220–230, https://doi.org/10.1017/aog.2019.10, 2019.

Sigrist, C.: Measurement of fracture mechanical properties of snow and application to dry snow slab avalanche release, Ph.D. thesis, ETH Zurich, Zürich, https://doi.org/10.3929/ethz-a-005282374, 2006.

Srivastava, P. K., Chandel, C., Mahajan, P., and Pankaj, P.: Prediction of anisotropic elastic properties of snow from its microstructure, Cold Regions Science and Technology, 125, 85 – 100, https://doi.org/https://doi.org/10.1016/j.coldregions.2016.02.002, http://www.sciencedirect.com/science/article/pii/S0165232X16300052, 2016.

Thomsen, L.: Weak elastic anisotropy, GEOPHYSICS, 51, 1954–1966, https://doi.org/10.1190/1.1442051, https://doi.org/10.1190/1.1442051, 1986.

Torquato, S.: Random Heterogeneous Media: Microstructure and Improved Bounds on Effective Properties, Applied Mechanics Reviews, 44, 37–76, https://doi.org/10.1115/1.3119494, https://doi.org/10.1115/1.3119494, 1991.

Torquato, S.: Effective stiffness tensor of composite media—I. Exact series expansions, Journal of the Mechanics and Physics of Solids, 45, 1421 – 1448, https://doi.org/https://doi.org/10.1016/S0022-5096(97)00019-7, http://www.sciencedirect.com/science/article/pii/S0022509697000197, 1997.

Torquato, S.: Effective stiffness tensor of composite media : II. Applications to isotropic dispersions, Journal of the Mechanics and Physics of Solids, 46, 1411 – 1440, https://doi.org/https://doi.org/10.1016/S0022-5096(97)00083-5, http://www.sciencedirect.com/science/article/pii/S0022509697000835, 1998.

Torquato, S.: Random Heterogeneous Materials: Microstructure and Macroscopic Properties, vol. 55, Springer, https://doi.org/10.1115/1.1483342, 2002a.

Torquato, S.: Statistical Description of Microstructures, Annual Review of Materials Research, 32, 77–111, https://doi.org/10.1146/annurev.matsci.32.110101.155324, https://doi.org/10.1146/annurev.matsci.32.110101.155324, 2002b.

Wautier, A., Geindreau, C., and Flin, F.: Linking snow microstructure to its macroscopic elastic stiffness tensor: A numerical homogenization method and its application to 3-D images from X-ray tomography, Geophysical Research Letters, 42, 8031–8041, https://doi.org/https://doi.org/10.1002/2015GL065227, https://agupubs.onlinelibrary.wiley.com/doi/abs/10.1002/2015GL065227, 2015.

Wautier, A., Geindreau, C., and Flin, F.: Numerical homogenization of the viscoplastic behavior of snow based on X-ray tomography images, The Cryosphere, 11, 1465–1485, 2016.

Weng, G.: Explicit evaluation of Willis' bounds with ellipsoidal inclusions, International Journal of Engineering Science, 30, 83 – 92, https://doi.org/https://doi.org/10.1016/0020-7225(92)90123-X, http://www.sciencedirect.com/science/article/pii/002072259290123X, 1992.

Willis, J.: Variational and Related Methods for the Overall Properties of Composites, vol. 21 of *Advances in Applied Mechanics*, pp. 1 – 78, Elsevier, https://doi.org/https://doi.org/10.1016/S0065-2156(08)70330-2, http://www.sciencedirect.com/science/article/pii/S0065215608703302, 1981.

Wu, F., Li, J., Geng, W., and Tang, W.: A VTI anisotropic media inversion method based on the exact reflection coefficient equation, Frontiers in Physics, 10, https://doi.org/10.3389/fphy.2022.926636, https://www.frontiersin.org/articles/10.3389/fphy.2022.926636, 2022.

Zysset, P. and Curnier, A.: An alternative model for anisotropic elasticity based on fabric tensors, Mechanics of Materials, 21, 243 – 250, https://doi.org/https://doi.org/10.1016/0167-6636(95)00018-6, http://www.sciencedirect.com/science/article/pii/0167663695000186, 1995.

Zysset, P. K.: A review of morphology–elasticity relationships in human trabecular bone: theories and experiments, Journal of Biomechanics, 36, 1469 – 1485, https://doi.org/https://doi.org/10.1016/S0021-9290(03)00128-3, http://www.sciencedirect.com/science/article/pii/S0021929003001283, bone Cell and Tissue Mechanics, 2003.

665